Numerical study on hypersonic aerodynamic characteristics of the high-pressure capturing wing configuration with wing dihedral

Siyuan Chang [a], Yao Xiao [a,b,*], Guangli Li [a,b], Zhongwei Tian [c], Kai Cui [a,b]

[a] State Key Laboratory of High-Temperature Gas Dynamics, Institute of Mechanics, Chinese Academy of Sciences, Beijing 100190, PR China
[b] School of Engineering Science, University of Chinese Academy of Sciences, Beijing 100049, PR China
[c] Wide Field Flight Engineering Science and Application Center, Institute of Mechanics, Chinese Academy of Sciences, Beijing 100190, PR China

ARTICLE INFO

ABSTRACT

High-pressure capturing wing (HCW) configuration is a potential hypersonic aerodynamic configuration that can simultaneously have good lift-drag characteristics with a large volumetric ratio. The effects of wing dihedral angle on the hypersonic aerodynamic characteristics of a conceptual HCW configuration with two lifting wings are investigated in this paper. Specifically, the dihedral angles of two wings, the upper HCW and the conventional delta wing at the bottom of the body, were regarded as the design variables with a given space. Furthermore, the uniform experimental design method, computational fluid dynamics simulation techniques, and kriging surrogate model algorithm were successively utilized to establish the distributions of aerodynamic parameters over the design space. The results indicate that the lift, drag, and lift-to-drag ratio (L/D) have the similar variation trends as the dihedral angles of the two wings change, and are more sensitive to the positive dihedral angle of the delta wing. When the angle of attack is small, the increasing positive dihedral angle significantly reduces L/D, but as the negative dihedral angle increases, L/D will first increase slightly and then decrease slowly. In particular, when the angle of attack is large, the wing dihedral angles have less influence on L/D. For the longitudinal stability, it is mainly affected by the dihedral angles of the delta wing, and the positive dihedral angle can slightly weaken it, while the negative one hardly changes it. The directional stability can be enhanced by the wing dihedral angles, especially the negative angle. The positive dihedral angle can improve the lateral stability, while the negative weaken it. However, when the angle of attack is large, the large positive dihedral angle of the delta wing may lead to a decrease in the lateral stability.

1. Introduction

Aerodynamic shape optimization design is one of the key technologies for hypersonic vehicles with long time flying in near space. Numerous hypersonic configurations with good lift-to-drag ratio (L/D) have been developed since the 1950s, such as lifting-body [1], blended-wing-body [2,3], and waverider [4–7] configurations. In fact, under hypersonic flight conditions, the wave drag and friction drag of vehicles will increase sharply, resulting in a so-called "L/D barrier" [8]. The contradictions between various aerodynamic performance parameters, such as between internal loading space and L/D, become increasingly prominent, which profoundly affects the shape design of hypersonic vehicles. At present, the multi-objective optimization design [9,10] is commonly utilized to mitigate these contradictions for hypersonic vehicles. However, this approach is essentially a trade-off between various performance parameters depending on different flight missions, typically resulting in sacrificing some minor items in exchange for an increase in overall performance.

Recently, in order to alleviate the design contradiction between volumetric ratio, lift, and L/D, to some extent, Cui et al. [11,12] proposed a novel aerodynamic configuration solution, namely the high-pressure capturing wing (HCW). Its core idea is to install a special lifting thin wing at a suitable position on the back of a large-volume fuselage body, and make full use of the high-pressure zone generated by the interaction between the body shock wave and the thin wing to provide a large lift compensation, thereby significantly improving L/D of the whole aircraft. After several years of development, the research speed domain of HCW configurations has extended from early hypersonic [11–13] to subsonic, transonic, and supersonic speeds [14–16], and numerous shapes have been tried and evaluated

* Corresponding author.
  E-mail address: xiaoyao@imech.ac.cn (Y. Xiao).

numerically/experimentally as the fuselage body, such as the single spinning-body [12,17], lifting-body [18], and waverider [12,19]. In 2019, Li et al. [19] conducted the wind tunnel tests at Mach number 6 for a waverider-HCW combination configuration. The results show that the volumetric ratio, maximum L/D, and corresponding lift coefficient are increased by about 10%, 6%, and 86%, respectively, compared with the high performance waverider configuration designed by Miller et al. [20], which strongly demonstrates the aerodynamic performance potential of this HCW configuration with double-lifting surfaces.

However, although these studies have demonstrated that this configuration has great advantages in balancing a large volumetric ratio, a high L/D, and a high lift coefficient in the hypersonic state, the performance required by other design disciplines, such as aerodynamic stability, must also be "good" while considering the practical engineering applications. Unfortunately, an increase in L/D may be prone to result in an unexpected deterioration in stability and maneuverability [21]. In fact, when a hypersonic vehicle is flying for a long time in near space, on the one hand, the aerodynamic control force or moment of the vehicle is limited due to the relatively rare atmosphere, and on the other hand, the design of control rudder surfaces yields great limitations considering that the vehicle faces an extreme thermal environment. Hence, maintaining usable stability and maneuverability has become a design bottleneck to improving hypersonic vehicle performance. It is necessary to investigate the effect of the aerodynamic shape design of this novel HCW configuration on the stability, particularly in the hypersonic state.

The stability investigation of HCW configurations consists of two aspects: longitudinal and lateral-directional stability. Recently, Chang et al. [22] performed numerical study on the longitudinal stability characteristics for a HCW aircraft with double-lifting surfaces in the hypersonic state, and specifically, the effects of uncertainty in flight attitude, inflow conditions, and center-of-gravity position on the longitudinal static and dynamic characteristics were evaluated based on the stability derivatives. However, at present there is still a gap in research on the lateral-directional stability characteristics of HCW configurations. For the conventional hypersonic vehicles with single-lifting surface, they are prone to have poor lateral-directional stability and have strong mutual constraints between lateral-directional and longitudinal stability characteristics [23]. Thus, for the novel HCW configurations with double-lifting surfaces, it is important to investigate the influence of aerodynamic shapes on lateral-directional stability characteristics.

In aerodynamic shape design of hypersonic vehicles, several geometric features such as vertical tail, ventral fin, and wing dihedral angle are associated with lateral-directional stability. Particularly, the wing dihedral angles typically have significant effect on lateral-directional stability by changing the spanwise distribution of aerodynamic force on wings, which has been numerically investigated by some researchers [24–27]. When studying the influence of wing dihedral angles on the stability of HCW configurations with double-lifting surfaces, a reasonable simplification of the geometric shape, especially the two wings, may be required. Specifically, for the wing directly attached to the fuselage, it can be simplified as a delta wing with a large sweep angle, which is a typical option for the aerodynamic investigations of both high and low speed aircrafts [28–32]. Moreover, for the HCW, it can be simplified as a flat plate with equal thickness, which has been implemented in the previous research work [14–16,33].

This study aims to numerically investigate the consequences of dihedral angles for the hypersonic aerodynamic characteristics of a conceptual HCW configuration with double-lifting surfaces. The paper is organized as follows. In Section 2, a more detailed introduction of the conceptual HCW configuration designed based on the basic principles of HCW aerodynamic configuration is given, and the consideration and design of wing dihedral angles are also illustrated. Further, several analysis methodologies such as experimental design method, numerical simulation techniques, and surrogate model are introduced in Section 3 to reveal the variation laws of different aerodynamic performance parameters that are shown and discussed in Section 4. Moreover, the
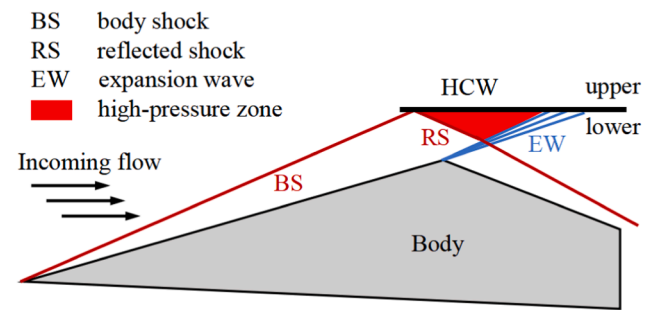

Fig. 1. Schematic of the HCW basic principle.
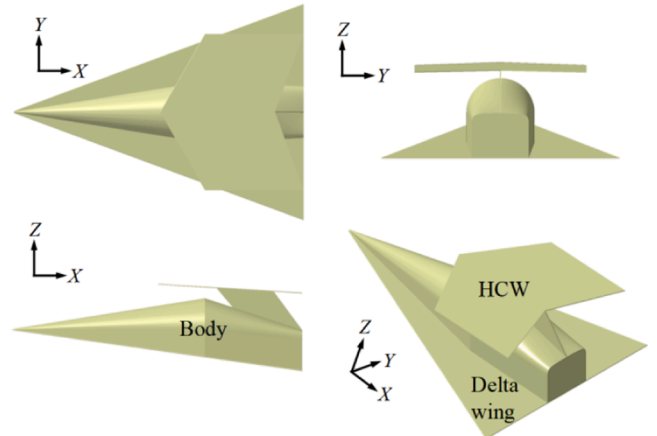

Fig. 2. Three-dimensional view of the baseline HCW configuration.

typical flow field characteristics effected by wing dihedral angles are also analyzed in Section 4. Finally, in Section 5 our conclusions on the main findings are put forward.

2. Principle and configuration

2.1. Basic principle of the high-pressure capturing wing

The HCW aerodynamic configuration can improve the aerodynamic performance by judiciously utilizing the beneficial shock wave interactions, and its basic design principle is shown in Fig. 1. The body shock wave is generated when the high-speed incoming flow is violently compressed by the raised upper surface of the body. A thin wing (hereinafter referred to as HCW) is installed at a suitable location above the body to capture the body shock wave and induce the reflected shock wave. Thus, the incoming flow, strongly compressed by two shock waves, will create a significant high-pressure zone on the lower surface of HCW. In addition, since HCW is approximately parallel to the incoming flow, the pressure on its upper surface is relatively small, basically comparable to the pressure of the incoming flow.

On the one hand, there is a large pressure difference between the upper and lower surfaces of HCW, which can significantly increase the lift of the vehicle. On the other hand, since HCW is relatively thin, the increase in drag caused by it is limited, so L/D of the whole aircraft is significantly improved. It is worth noting that the shape of the body must be reasonably designed to effectively prevent the reflected shock wave from causing large adverse interactions with the rear body.

### 2.2. Baseline high-pressure capturing wing configuration

In order to facilitate the calculation and analysis, a parametric conceptual configuration is designed based on the aforementioned HCW

Table 1

Main geometric parameters of the baseline HCW configuration.

Component	Geometric parameter	Value
Body	Axial length (L)	1000 mm
Body	Upper surface compression angle	9°
Body	Lower surface compression angle	6°
Body	Longitudinal expansion angle of the rear segment	18°
Delta wing	Sweep angle	70°
HCW	Axial length	490 mm
HCW	Half-span length	400 mm
HCW	Sweep angle of leading edge	30°
HCW	Sweep angle of trailing edge	20°
HCW	Setting angle relative to the X-axis	3.5°
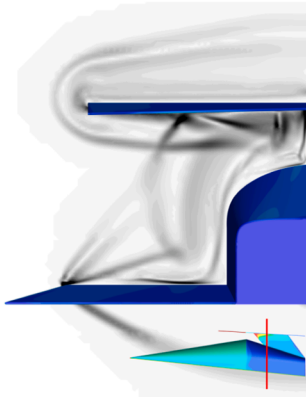
(a) numerical schlieren image on the slice $X = 0.8L$
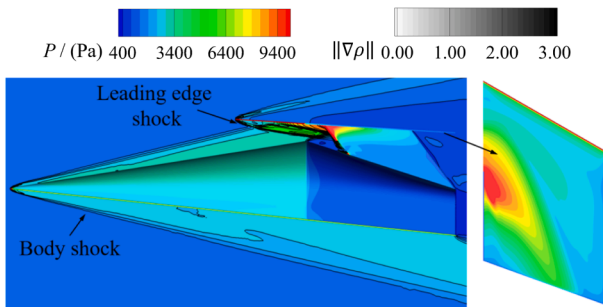
(b) pressure contours on the surface and the longitudinally symmetric slice
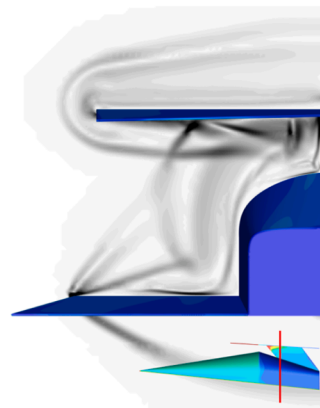
(c) numerical schlieren image on the slice $X = 0.8L$

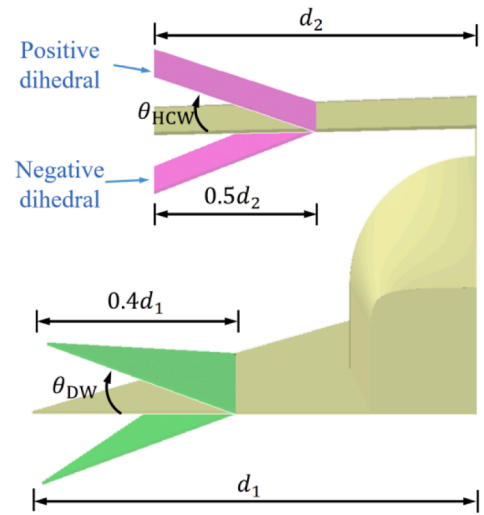**Fig. 3.** CFD results for the baseline HCW configuration at $\alpha = 0°$ and $\beta = 0°$.

Fig. 4. Schematic of the wing dihedral angles for the delta wing and HCW.

Table 2

Design variables and space.

Design variables	Lower bound (°)	Upper bound (°)
θ_{DW}	−50	50
θ_{HCW}	−20	20

basic principle as the baseline configuration in this paper. As shown in Fig. 2, the baseline configuration includes two lifting wings, i.e., the upper HCW and the delta wing at the bottom of the body, in which HCW is connected to the rear body by a single support, and the delta wing is directly connected to the lower surface of the body. In addition, both the two wings and the support are flat plates of equal thickness with straight leading edges, all with a 1 mm passivation radius. The baseline HCW configuration has no control rudder surface, and its some main geometric parameters are listed in Table 1. Furthermore, the computational fluid dynamics (CFD) numerical techniques are performed to obtain the flow field, as shown in Fig. 3, under the design condition (the flight Mach number is $M = 6$, flight altitude is $H = 30$km, and both the angle of attack α and sideslip angle β are 0°). The results show that the baseline configuration satisfies the HCW basic principle.

2.3. High-pressure capturing wing configuration with wing dihedral

In order to investigate the influence of the wing dihedral angle on the aerodynamic characteristics, it is necessary to perform parametric modeling of the configuration with wing dihedral based on the above baseline HCW configuration. Starting from the wing tips of the delta wing and HCW, the appropriate width is taken in the spanwise direction to deflect the wing upward and downward, respectively, as shown in Fig. 4. As an important parameter, the width of the deflection section should be neither too small nor too large: if it is too small, it may not reflect the effect of the wing dihedral angle on the aerodynamic performance; if it is too large, it cannot be designed due to the constraints of the vehicle layout. After comprehensive consideration, the deflection section widths of the delta wing and HCW are taken to be 0.4 and 0.5 times of their half-span length (d_1 and d_2), respectively.

In this paper, the dihedral angles of the delta wing and HCW are represented by θ_{DW} and θ_{HCW}, respectively. Note that the dihedral angle is positive when the wing is deflected upward, and negative when the wing is deflected downward. Table 2 lists the upper and lower bounds of the two design variables, i.e., the design space. Thus, the baseline HCW configuration corresponds to $\theta_{DW} = \theta_{HCW} = 0°$ Moreover, the aerodynamic coupling between the delta wing and HCW is usually required
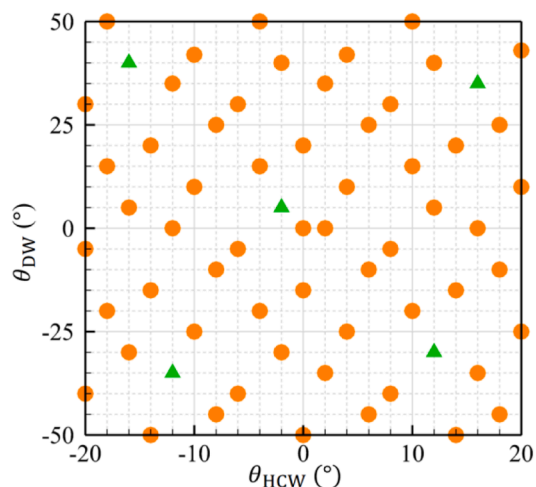
Fig. 5. Experimental design sample point distribution (Orange circle: training sample; green delta: test sample).
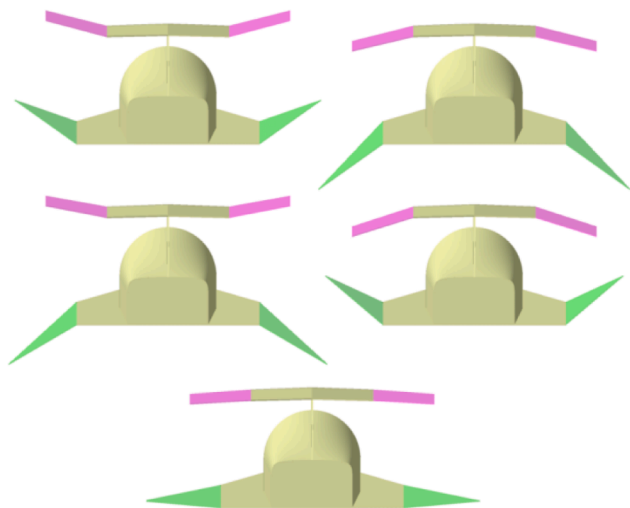

Fig. 6. Five test samples of HCW configurations.

to be as small as possible in the aerodynamic configuration design of the HCW configuration, and the adverse aerodynamic interference between the two wings is likely to occur when the negative dihedral angle of HCW is too large. Hence, HCW is studied in a relatively small range of dihedral angle.

3. Methodology and modeling

The analysis process in this paper is as follows: first, according to the determined design variables and their design space, a uniform experimental design method is used to generate the design variable set, and then a series of sample HCW configurations with different wing dihedral angles can be obtained. Second, based on the automatic mesh generation script, the mesh generation of all the sample configurations can be completed in batches. Then, the CFD solver is used to conduct numerical simulation of typical conditions for all sample configurations, and the corresponding aerodynamic performance parameters are extracted to construct the aerodynamic data set. Finally, the kriging method is used to obtain the different models of aerodynamic parameters, which is beneficial to investigate the variation laws of aerodynamic parameters throughout the design space, and the influence of wing dihedral on the hypersonic aerodynamic characteristics of the HCW configuration can be analyzed in combination with typical flow field characteristics.

3.1. Experimental design method

In order to uniformly disperse the samples throughout the design space, which is helpful to construct a global high-fidelity input-output response model, the well-known uniform design method [34], is used in this paper. The uniform design is one of space filling designs and it seeks sample points to be uniformly scattered on the domain. Note that the uniform design requires all design points to be uniformly distributed in all dimensions, while the popular Latin hypercube sampling requires all design points to be uniformly distributed in each dimension [35]. In this study, 21 levels were set for each design variable according to the design space given in Table 2, and each level of the variable was repeated three times. Thus, 64 sample points (including the baseline configuration) were obtained, and their distribution is shown in Fig. 5.

Since it is often necessary to assess the accuracy of the approximation model based on the test samples, the 64 sample points were further divided into two parts: 59 training samples and 5 test samples, which are distinguished by different color and shape scatters, as shown in Fig. 5. Furthermore, Fig. 6 shows the corresponding HCW configurations for the test samples, which have significantly different wing dihedral combinations.

3.2. Numerical simulation techniques and grid dependency study

In this study, for each HCW configuration mentioned in Section 3.1, we access their aerodynamic performances under the following conditions: the flight Mach number is $M = 6$, flight altitude is $H = 30$km, angles of attack are $\alpha = 0,\ 5,\ 10°$, and sideslip angles are $\beta = 0,\ 2°$ When hypersonic vehicles are flying for a long time in near space, certain effects and phenomena may occur, such as strong shock wave interactions, high aerodynamic heat fluxes, real gas effects, and rarefied gas effects. Note that the real gas effects and rarefied gas effects can be neglected in this study due to not very extreme flight speed and altitude. For the preliminary numerical analysis of rarefied gas effects on the flow structure and aerodynamic performance of the HCW configuration, readers are referred to the reference [36].

CFD techniques were used to evaluate the aerodynamic performance of all HCW configurations depicted in Fig. 5 by solving the three-dimensional compressible version of the Reynolds-averaged Navier-Stokes (RANS) governing equations. The CFD++ software (version 14.1.1) of Metacomp Technologies, Inc. [37] was conducted for this study. More specifically, the inviscid fluxes are solved using the Harten-Lax-van Leer-Contact (HLLC) scheme, and viscous fluxes are solved using the classic second-order centered scheme along with the Menter's two-equation Shear Stress Transport (SST) $k - \omega$ turbulence model. The discretization in space is performed using the second-order finite volume method, and the integration in time is employed using the implicit dual time-stepping algorithm. Previous studies have shown the fidelity of CFD++ in hypersonic aerodynamic problems [15,38,39]. Since this study is mainly concerned with the pressure distribution on the configuration surfaces rather than the heat flux distribution, the adiabatic wall boundary condition is set for the configuration surfaces. On the other hand, the reference area and length were taken as the top-down projection area and the total axial length of the baseline configuration, i.e., 0.368m^2 and 1m, respectively. The origin of the co-ordinate system (shown in Fig. 2) was located at the vertex of the body head, and the moment reference center was fixed at $[0.65,\ 0,\ 0]$m. In addition, a positive angle of attack was a nose-up position achieved through a positive rotation around the pitch axis (Y-axis in Fig. 2), and a positive sideslip angle was achieved by a negative rotation around the yaw axis (Z-axis in Fig. 2).

Before performing the CFD simulation for all the configurations, the influence of the computational grid on the results needs to be examined, i.e., a grid dependency investigation to ensure the reasonableness of the chosen grid scale. Here the HCW configuration with dihedral angle
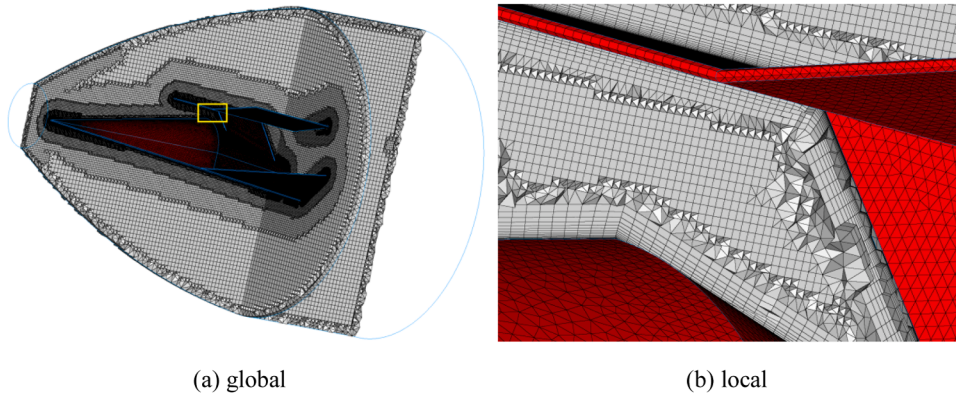
(a) global

(b) local

Fig. 7. Computational grid of the HCW configuration with $\theta_{DW} = 45°$ and $\theta_{HCW} = 20°$.

Table 3
Force and moment coefficients obtained using different grids at $\alpha = 10°$ and $\beta = 0°$.

Grid	C_L	C_D	C_m
G1	0.27462	0.08853	−0.00613
G2	0.27148	0.08987	−0.00598
G3	0.27091	0.08982	−0.00597

Table 4
Force and moment coefficients obtained using different grids at $\alpha = 10°$ and $\beta = 2°$.

Grid	C_Y	C_l	C_n	C_m
G1	0.00737	−0.00257	0.00120	−0.00611
G2	0.00746	−0.00262	0.00123	−0.00615
G3	0.00747	−0.00261	0.00122	−0.00614

Table 5
Refinement ratios and GCI for some force and moment coefficients at $\alpha = 10°$ and $\beta = 0°$.

Refinement level	r	$GCI(C_L)$ (%)	$GCI(C_D)$ (%)	$GCI(C_m)$ (%)
G1-G2	1.27	0.64	3.03	5.10
G2-G3	1.25	0.47	0.13	0.38

Table 6
GCI for some force and moment coefficients at $\alpha = 10°$ and $\beta = 2°$.

Refinement level	$GCI(C_Y)$ (%)	$GCI(C_l)$ (%)	$GCI(C_n)$ (%)	$GCI(C_m)$ (%)
G1-G2	2.45	3.88	4.96	1.32
G2-G3	0.30	0.86	1.85	0.37

$\theta_{DW} = 45°$ and $\theta_{HCW} = 20°$ was taken as a test example. The structured/ unstructured hybrid grid strategy was chosen to quickly generated grids considering the complexity of the configuration, as sketched in Fig. 7. Three grids (G1 to G3) of different refinement were performed in this grid dependency investigation. The corresponding grid-cell numbers were approximately 5000,000 (G1), 10,260,000 (G2), and 19,870,000 (G3), respectively. Note that both the configuration surface grid and the space grid are refined or coarsened. Considering that the computational accuracy of boundary layer flows is closely related to the height of the first layer of grid-cell, we vary this height during the generation of grids at different scales. Specifically, the heights of the first layer were 1×10^{-4}, 6×10^{-5}, and 3×10^{-5} m, corresponding to the maximum wall $Y+$ of 9.5, 5.5, and 2.7, respectively. It should be note that the wall in most regions has a $Y+$ value of less than 1.0, effectively resolving the boundary layer flow. There are a few regions where $Y+$ exceeds 1.0, primarily concentrated on the leading edges of the wings and support structure, which only slightly impacts the aerodynamic force/moment concerned in this paper.

The grid convergence index (GCI) [40] is employed for the evaluation of the accuracy of the results. The GCI represents how much a converged solution can change with further refinement and how far it is from the asymptotic range [41]. For three-dimensional problems, the refinement ratio of each subsequent grid can be calculated by Eq. (1), where N_i is the grid-cell number of the grid Gi.

$$r_{i,i+1} = \left(\frac{N_{i+1}}{N_i} \right)^{1/3} \tag{1}$$

Further, the GCI on each refinement level can be computed using Eq. (2), where F_s is a safety factor, set to 1.25 because more than two grids are used [42], f is the value of the examined parameter, and m is the order of accuracy, set to 2 for second-order discretization schemes.

$$GCI_{i,i+1} = F_s \frac{\left| \frac{f_i - f_{i+1}}{f_{i+1}} \right|}{r_{i,i+1}^m - 1} \tag{2}$$

The coefficients of lift, drag, and pitching moment (C_L, C_D, and C_m) obtained using the three grids at $\alpha = 10°$ and $\beta = 0°$ are presented in Table 3. The rolling, yawing, and pitching moment coefficients (C_l, C_n, and C_m) and lateral force coefficient (C_Y) calculated using the three grids

at $\alpha = 10°$ and $\beta = 2°$ are listed in Table 4. Additionally, the GCI values are computed for these aerodynamic parameters, and the results are presented in Tables 5 and 6. It is observed that the GCI for refinement level G2-G3 is very small for all the examined parameters. Together with the results presented in Tables 3 and 4, it is evident that solution is practically grid-independent for grids G2 and G3. Thus, all the investigations in the present study are performed with the G2 refinement level since any further refinement does not provide any significant benefit in terms of resolution and only increases the computational cost of the CFD computation.

To ensure that the solution of each CFD simulation is converged, along with the normalized RSM residuals, the axial and normal forces acting on the HCW configuration surface were monitored. As shown in Fig.8(a), the normalized RMS residuals demonstrate a monotonic behavior, for the first 3000 iterations, at which point the unscaled RMS residuals have decreased by five orders of magnitude. The development of the axial and normal forces depicted in Fig.8(b) is consistent for a predefined number of iterations (i.e., 1000). Therefore, the solution was considered converged.

3.3. Surrogate model and modeling accuracy

After obtaining the aerodynamic data set, a surrogate model can be used to establish the mapping relationship between the design variables
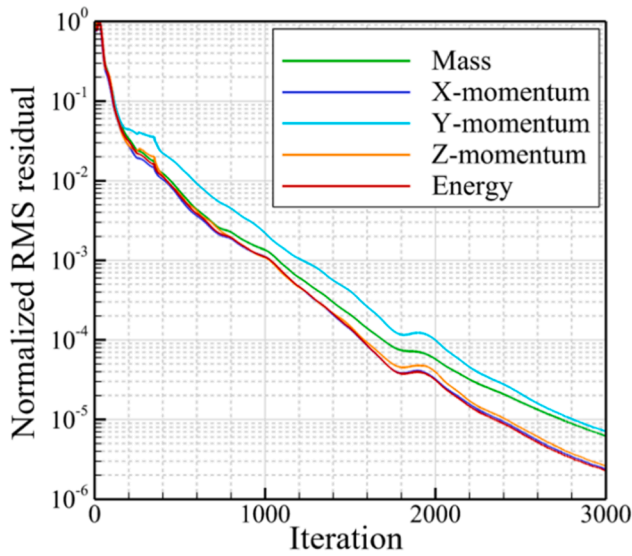
(a) normalized RMS residuals
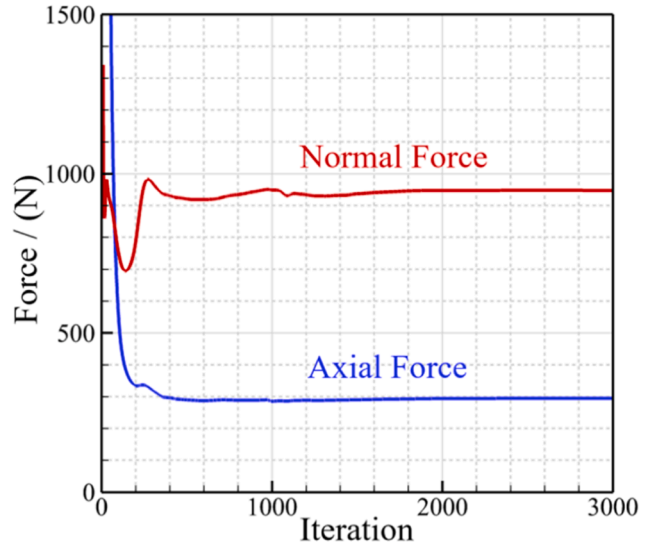
(b) aerodynamic forces

Fig. 8. Convergence of normalized RMS residuals and axial/normal forces acting on the HCW configuration with $\theta_{DW} = 45°$ and $\theta_{HCW} = 20°$.

and the objective function. There are various surrogate models, such as radial basis function model, kriging model, and artificial neural network model. Ordinary kriging (OK) [43], the most widely used kriging method, was used in this paper to establish the relationship between wing dihedral angles and each aerodynamic parameter at different states. Its formula can be simply expressed as:

$$\widetilde{Z}(x_0) = \sum_{i=1}^{n} \omega_i Z(x_i) \tag{3}$$

where $\widetilde{Z}(x_0)$ is a linear estimation of the true value $Z(x_0)$ at the point location x_0, using the data values $Z(x_i)$ from n neighboring sample points x_i with corresponding weights ω_i. The ordinary kriging method is characterized by making ω_i satisfy unbiased estimations:

$$\sum_{i=1}^{n} \omega_i = 1 \tag{4}$$

Moreover, the variance of the estimation error should be minimum, i. e.,

$$\min_{\omega_i} S = \min_{\omega_i} Var[\widetilde{Z}(x_0) - Z(x_0)] \tag{5}$$

Then, the first-order partial derivative of S can be computed for each weight ω_i, and let all the partial derivatives be equal to 0, so that a set of equations can be obtained to further calculate n weights ω_i.

To examine the accuracy of the ordinary kriging model used for aerodynamic parameters, the mean absolute error (MAE) and the mean relative error (MRE) are adopted as the error criteria. Specifically, for each aerodynamic parameter y at a certain state, the MAE and MRE criteria can be defined as Eq. (6), where y_{CFD} and y_{OK} are the values of the target parameter obtained using the CFD solver and OK model, respectively, n is the number of test samples, and $\widehat{y}_{CFD}^{max}$ and $\widehat{y}_{CFD}^{min}$ are the maximum and minimum values of the target parameter obtained using the CFD solver in the whole training set, respectively.

$$y_{MAE} = \frac{1}{n} \sum_{i=1}^{n} |y_{CFD} - y_{OK}|_i$$

$$y_{MRE} = \frac{y_{MAE}}{\widehat{y}_{CFD}^{max} - \widehat{y}_{CFD}^{min}} \times 100\% \tag{6}$$

Table 7
Test errors of different aerodynamic parameters at different angles of attack.

Parameter	α (°)	MAE	MRE (%)
C_L	0	4.0E-5	0.21
C_L	5	1.8E-4	0.51
C_L	10	2.8E-4	0.48
C_D	0	4.0E-5	1.61
C_D	5	2.0E-5	0.25
C_D	10	1.6E-4	0.86
$C_{l\beta}$	0	3.6E-4	0.44
$C_{l\beta}$	5	4.2E-4	0.38
$C_{l\beta}$	10	6.6E-4	0.47
$C_{n\beta}$	0	4.0E-4	1.67
$C_{n\beta}$	5	8.2E-4	2.89
$C_{n\beta}$	10	1.1E-3	2.77
X_{ac}	0	4.2E-4	1.24
X_{ac}	5	2.0E-4	0.48

It should be note that the conventional relative error criterion is the ratio between the absolute error and the CFD result; obviously, if the individual CFD result is close to 0, the ratio may be an undesired large value. In order to avoid this abnormal situation, we use the overall change amplitude of the target parameter in the training set to calculate MRE.

Table 7 presents the test errors of C_L, C_D, rolling moment derivative $C_{l\beta}$, yawing moment derivative $C_{n\beta}$, and dimensionless aerodynamic center position X_{ac}, at different angles of attack. For MAE, the values are basically in the order of 10^{-4}, and some even reach the order of 10^{-5}; for MRE, the maximum value is 2.89%, corresponding to $C_{n\beta}$ at $\alpha = 10°$ In brief, the modeling accuracy is sufficient to support the following analysis.

4. Results and analysis

4.1. Lift-drag characteristics

The distribution contours of lift coefficient, drag coefficient, and L/D for the entire configuration over the design space at three angles of attack are presented in Figs. 9 and 10, where the horizontal and vertical coordinates indicate the dihedral angles of HCW and delta wing, respectively, and the contour values represent the variations relative to
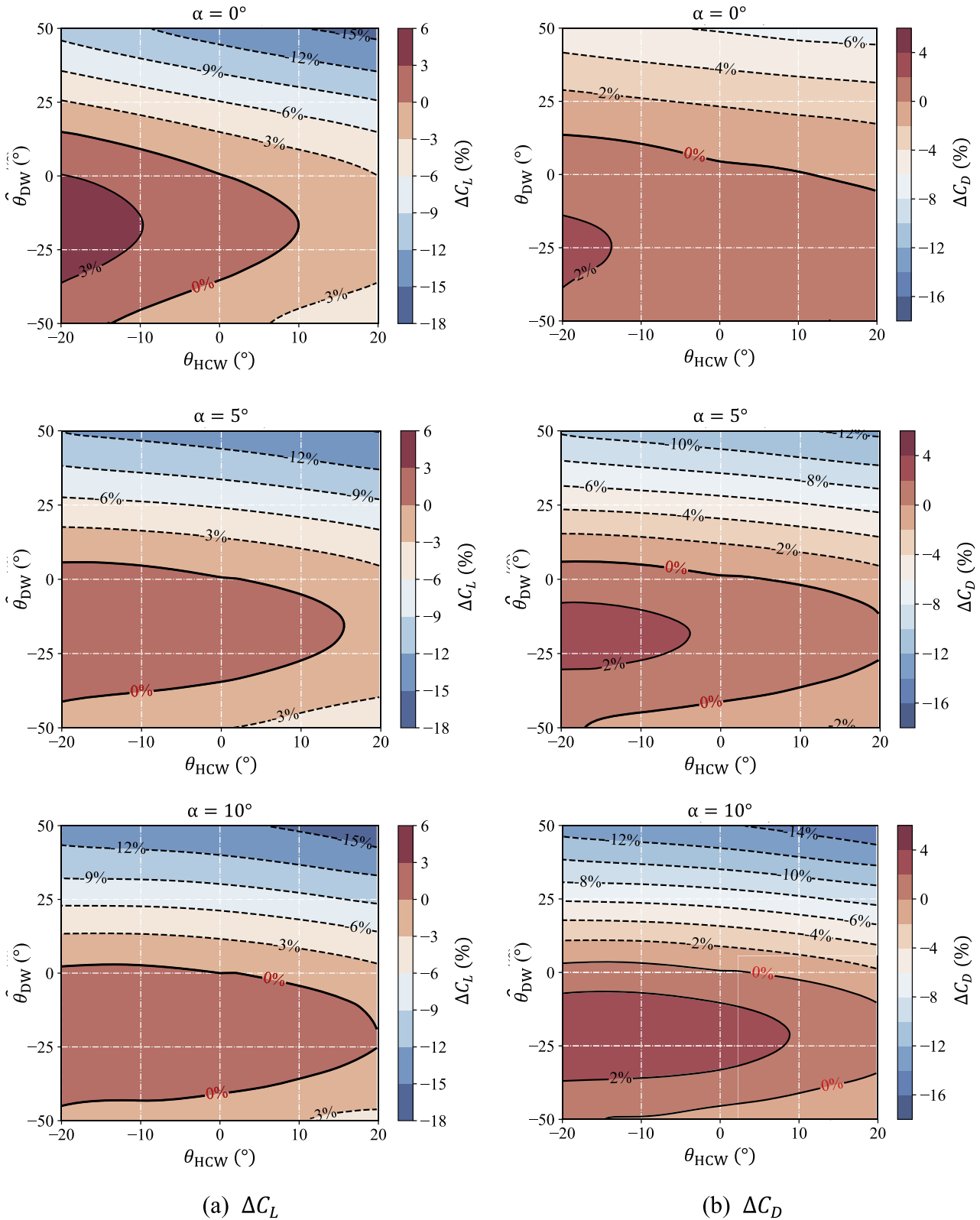
Fig. 9. Percentages of variation in lift and drag coefficient over the design space at different angles of attack.

the results corresponding to the baseline HCW configuration.

The lift coefficient distribution in Fig. 9(a) illustrates that increasing the negative dihedral angle of HCW will slightly improve the lift coefficient. Moreover, the delta wing with an appropriate negative dihedral angle will be beneficial to increase the lift coefficient, but if the angle is

too large, the lift coefficient will be reduced instead. As the angle of attack increases, the lift coefficient becomes less sensitive to the changes in the dihedral angle of HCW, and more sensitive to changes in the dihedral angle of the delta wing (especially the positive angle). For this configuration, the maximum increase in the lift coefficient throughout
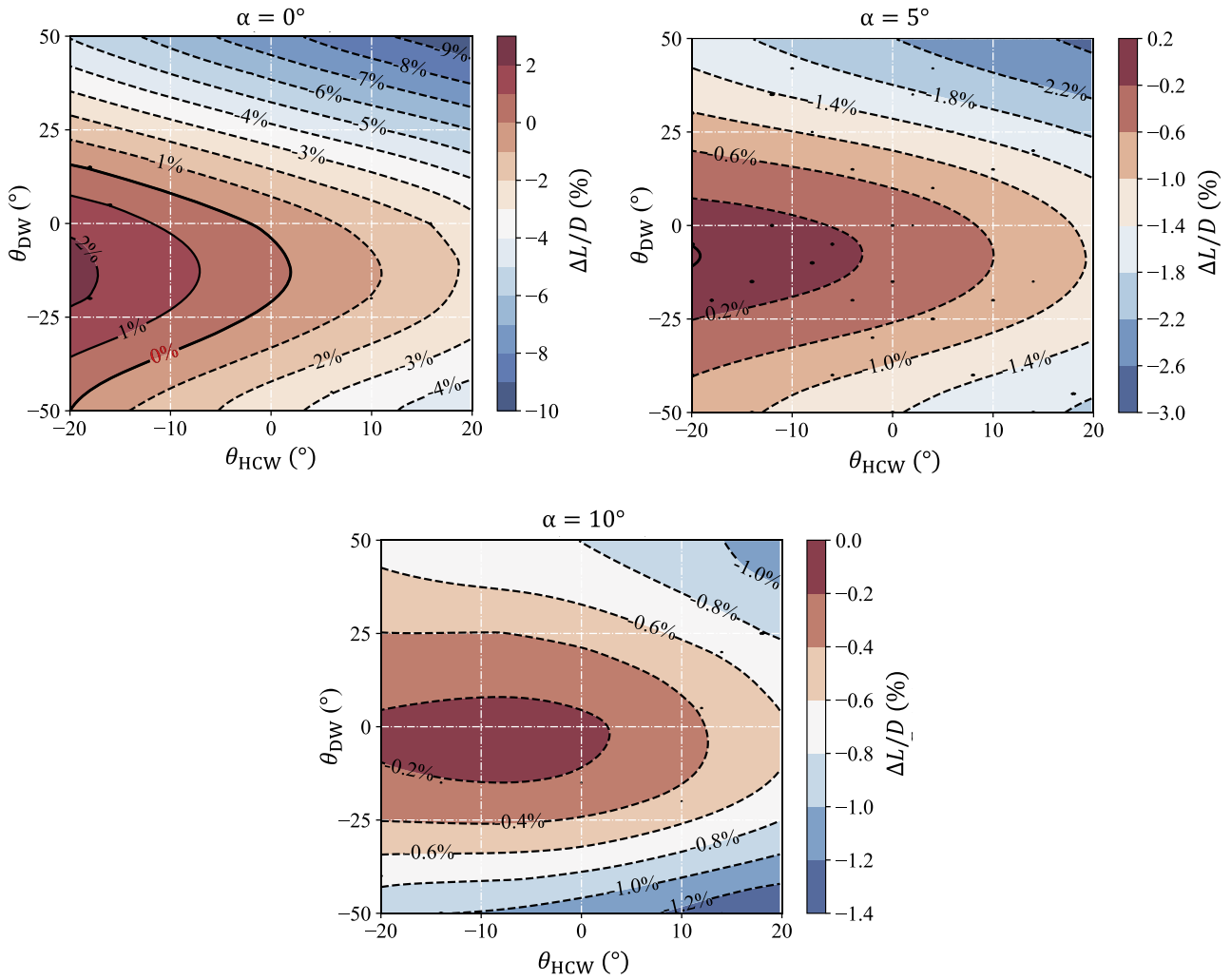
Fig. 10. Percentages of variation in L/D over the design space at different angles of attack.

the design space corresponds to approximately $\theta_{DW} = -20°$ and $\theta_{HCW} = -20°$, while the large positive dihedral angles of the delta wing and HCW will significantly reduce the lift coefficient by a maximum of approximately 15% even at different angles of attack.

The variation tread of the drag coefficient over the design space is generally consistent with that of the lift coefficient, as shown in Fig. 9 (b). Differently, as the angle of attack increases from 0° to 10°, the maximum reduction in the drag coefficient over the design space
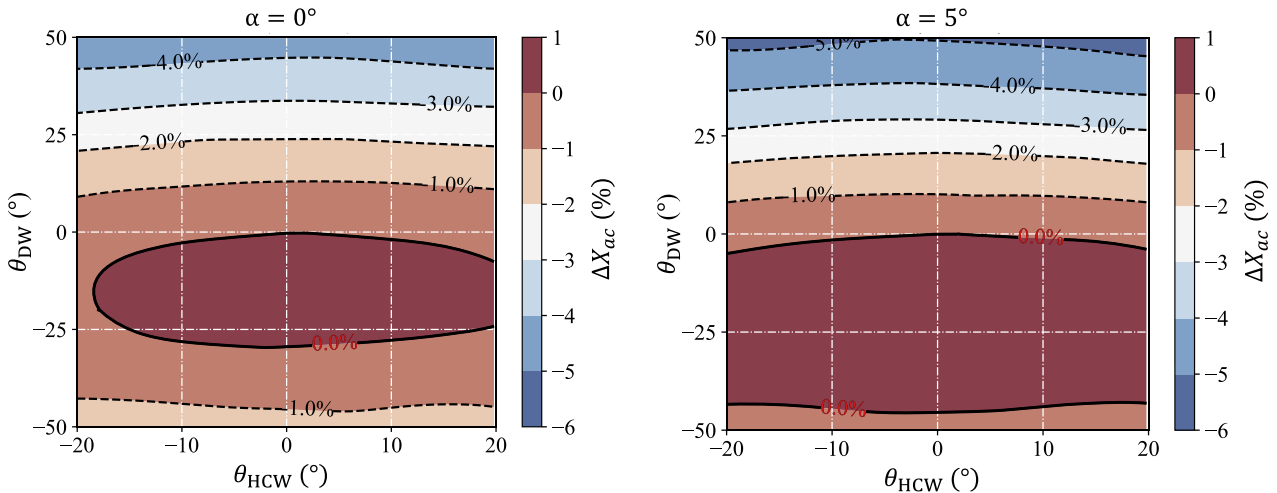

Fig. 11. Percentages of variation in dimensionless aerodynamic center position over the design space at different angles of attack.
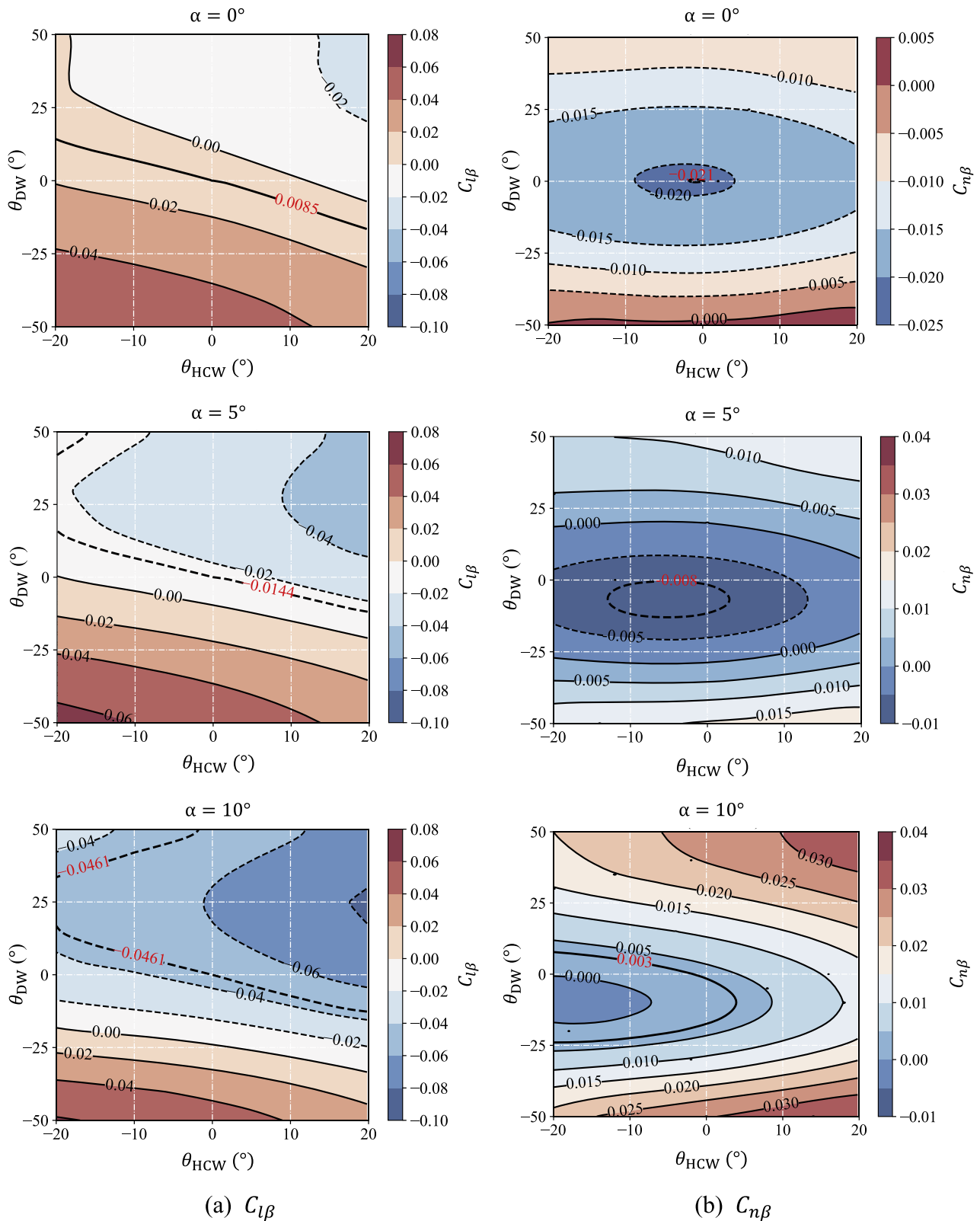
Fig. 12. Rolling and yawing moment derivative over the design space at different angles of attack.

changes from 6% to 15%. In other words, the sensitivity of the drag coefficient to the wing dihedral (especially for the delta wing) increases significantly with the increase of the angle of attack.

From the L/D distribution in Fig. 10, it can be seen that the influence of the wing dihedral angle on L/D is significantly weakened with

increasing the angle of attack, e.g., the maximum change is about −9% at $\alpha = 0°$, while about −1.2% at $\alpha = 10°$ For this configuration, the maximum increase in L/D at $\alpha = 0°$ throughout the design space corresponds to approximately $\theta_{DW} = -15°$ and $\theta_{HCW} = -20°$, with an increase of about 2%.

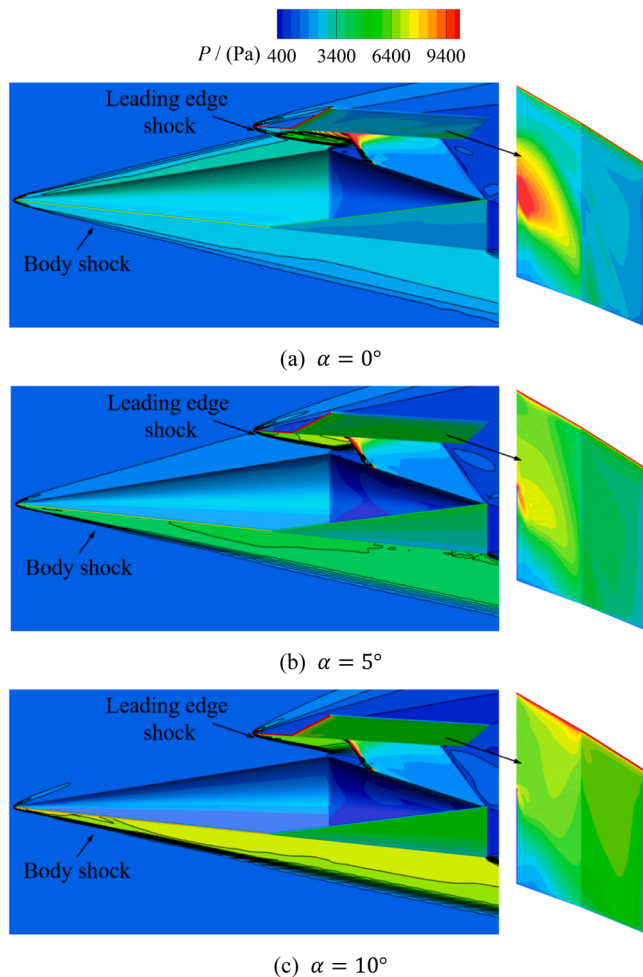(a) $\alpha = 0°$

(b) $\alpha = 5°$

(c) $\alpha = 10°$

Fig. 13. Pressure contours on the surfaces and longitudinal symmetrical plane for the HCW configuration with $\theta_{DW} = 40°$ and $\theta_{HCW} = 20°$ at different angles of attack ($\beta = 0°$).

4.2. Longitudinal stability

In this section, the influence of the wing dihedral angle on the longitudinal static stability of this configuration is studied, using the dimensionless aerodynamic center position X_{ac} as a criterion. When the aerodynamic center moves backwards, i.e., X_{ac} increases, the longitudinal static stability is enhanced; otherwise, it is weakened.

As can be seen from the distribution of the dimensionless aerodynamic center position in Fig. 11, the longitudinal static stability is more sensitive to the dihedral angle of the delta wing (especially the positive angle), and is basically unaffected by the dihedral angle of HCW. Specifically, for the delta wing, when its positive dihedral angle increases, the longitudinal static stability is weakened; when its negative dihedral angle is very large, the longitudinal static stability is slightly enhanced. Moreover, as the angle of attack increases, the impact of the negative dihedral angle of the delta wing on the longitudinal static stability is further diminished.

4.3. Lateral-directional stability

In this study, the rolling moment derivative $C_{l\beta}$ and the yawing moment derivative $C_{n\beta}$ are used as criteria to evaluate the effects of the wing dihedral angle on the lateral and directional static stability of this configuration, respectively. Under the coordinate system shown in Fig. 2, $C_{l\beta} < 0$ represents the lateral static stability, and the smaller the value of $C_{l\beta}$, the stronger the lateral static stability; $C_{n\beta} > 0$ indicates the

directional static stability, and the larger the value of $C_{n\beta}$, the stronger the directional static stability.

The distributions of $C_{l\beta}$ and $C_{n\beta}$ over the design space at three angles of attack are shown in Fig. 12, and for ease of comparison, the red values in each figure indicate the results corresponding to the baseline HCW configuration.

As can be seen in Fig. 12(a), the lateral static stability is weakened as the negative dihedral angle of the HCW or delta wing increases. In addition, with the increase of the positive dihedral angle of the delta wing, the lateral static stability presents an initial increase and then decrease trend, especially at the large angle of attack. Overall, the lateral static stability is more sensitive to negative than to positive dihedral angles. Specifically, for the configuration in this study, the strongest lateral static stability at $\alpha = 10°$ throughout the design space corresponds to approximately $\theta_{DW} = 25°$ and $\theta_{HCW} = 20°$

From the yawing moment derivative distributions in Fig. 12(b), it can be observed that at $\alpha = 0°$, increasing the positive or negative dihedral angle of the HCW or delta wing is beneficial to improve the directional static stability. However, at a larger angle of attack, a slight decrease in the directional static stability occurs when both the HCW and delta wing have a small negative dihedral angle. Particularly, at different angles of attack, the negative dihedral of the delta wing is more effective in improving the directional static stability than the positive dihedral.

4.4. Flow field characteristics

To further explore the influence mechanism of wing dihedral angles on the hypersonic aerodynamic performance of HCW configurations, this section focuses on the flow field characteristics acting on several typical HCW configurations with wing dihedral.

First, taking the HCW configuration with $\theta_{DW} = 40°$ and $\theta_{HCW} = 20°$ for example, Fig. 13 illustrates the pressure contours on its surface and longitudinal symmetrical plane at angles of attack $\alpha = 0°, 5°, 10°$ and sideslip angle $\beta = 0°$ At $\alpha = 0°$, two detached shock waves arising from the head of the fuselage and the leading edge of HCW, respectively, namely body shock and leading edge shock, dominate the main flow field structures. Particularly, the fan-shaped high-pressure zone on the lower surface of HCW shown in Fig. 13(a), caused by the interaction between the body shock and HCW, significantly affects the aerodynamic forces acting on the HCW. By contrast, the body shock above the fuselage becomes weaker as the angle of attack increases, while the leading edge shock becomes stronger. Since the compression angle of the upper surface of the fuselage is 9°, the expansion wave instead of the shock wave is induced at $\alpha = 10°$ as shown in Fig. 13(c). Note that the pressure distribution on the lower surface of HCW at $\alpha = 10°$ is significantly influenced by the leading edge shock, which is obviously simpler than the case at $\alpha = 0°$ Moreover, for the delta wing, the pressure distribution on its lower surface is always affected by the body shock no matter how the angle of attack changes, which is similar to the situations encountered with most conventional hypersonic vehicles with single-lifting surface.

In view of the fact that the flow field structure below HCW is more complicated at small angles of attack, Fig. 14 shows the numerical schlieren (density gradient magnitude $\| \nabla \rho \|$) images on the slice $X = 800$mm for the HCW configurations with four dihedral angle combinations at $\alpha = 0°$ and $\beta = 0°$ The chosen dihedral angles of HCW are the bound values (20° and $-20°$), while the dihedral angles of the delta wing are close to the bound values, i.e., 40° and $-40°$ Comparison of the schlieren patterns obviously shows that the change of dihedral angle only significantly affects the flow structures near the wing tips, and the flow structures near the fuselage body and longitudinal symmetrical plane remain almost unchanged, even in Fig. 14(c) where the distance between the HCW and delta wing is relatively small. In other words, the flow field disturbances caused by the dihedral angle changes of the HCW and delta wing are basically independent of each other in this study. This
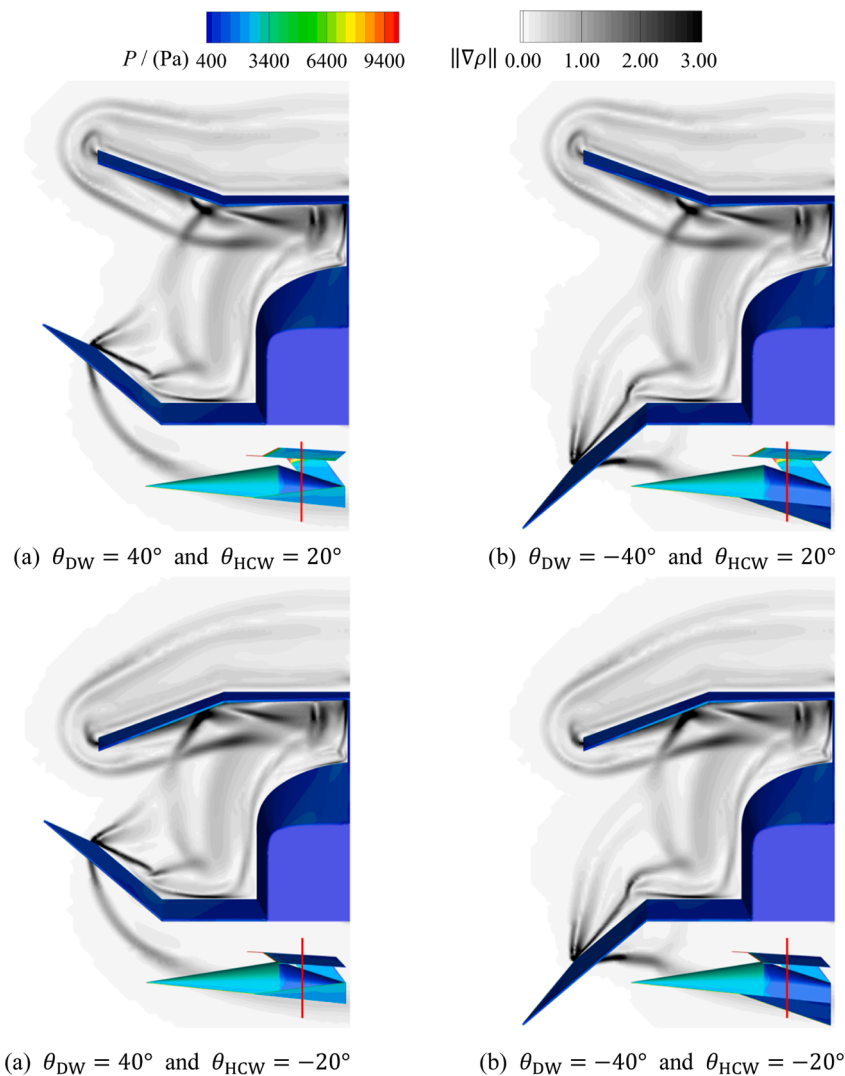
P / (Pa) 400 3400 6400 9400 $\|\nabla\rho\|$ 0.00 1.00 2.00 3.00

(a) $\theta_{DW} = 40°$ and $\theta_{HCW} = 20°$ (b) $\theta_{DW} = -40°$ and $\theta_{HCW} = 20°$

(a) $\theta_{DW} = 40°$ and $\theta_{HCW} = -20°$ (b) $\theta_{DW} = -40°$ and $\theta_{HCW} = -20°$

Fig. 14. Numerical schlieren images on the slice $X = 800$**mm** and pressure contours on the surface for the HCW configurations with different dihedral angles at **α** = 0° and **β** = 0°.

P / (Pa) 400 3400 6400 9400

$\theta_{HCW} = 20°$ $\theta_{HCW} = -20°$ $\theta_{HCW} = 20°$ $\theta_{HCW} = -20°$

(a) upper surface   (b) lower surface
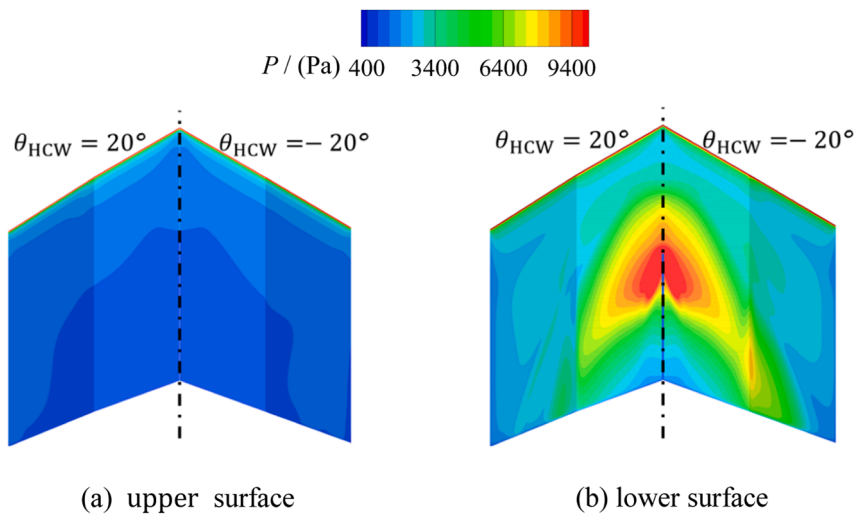
Fig. 15. Pressure contours on the upper and lower surfaces of the HCW at **α** = 0° and **β** = 0°.

(a) upper surface   (b) lower surface

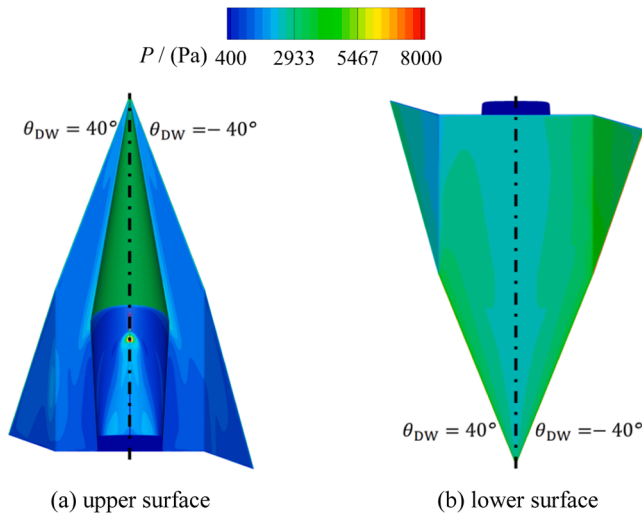**Fig. 16.** Pressure contours on the upper and lower surfaces of the delta wing at $\alpha = 0°$ and $\beta = 0°$.

is partly due to the inherently limited influence domain of hypersonic aerodynamic interference, and partly due to the fact that the vertical distance between the HCW and delta wing is not too small. Therefore, for the HCW and delta wing, the effects of their dihedral angle changes on the flow field characteristics and aerodynamic performance are analyzed separately in the following paper.

The pressure distributions on the upper and lower surfaces of HCW at $\alpha = 0°$ and $\beta = 0°$ are presented in Fig. 15, with a comparison of $\theta_{HCW} = 20°$ and $\theta_{HCW} = -20°$ The pressure level on the upper surface of HCW is smaller than that on the lower surface, caused by the expansion wave and nearly unaffected by the dihedral angle changes. Comparing with the results of the baseline HCW configuration shown in Fig. 3(a), the range of the high-pressure zone on the lower surface is expanded when HCW has a negative dihedral angle, and is reduced when HCW has a positive dihedral angle. In summary, when the dihedral angle of HCW changes, the pressure distribution on the lower surface changes more violently than that on the upper surface, which affects the lift-drag characteristics. More specifically, both the lift and drag coefficients increase if HCW has a negative dihedral angle, and decrease if HCW has a positive dihedral angle. Note that the high-pressure zone on the lower surface of HCW is mainly concentrated in the middle, while the variation in pressure distribution is limited, mainly in the area where the wing deflection occurs. This explains the limited impact of changing the HCW dihedral angle on the lift-drag characteristics illustrated in Fig. 9.

For the delta wing, the pressure distributions on its upper and lower surfaces at $\alpha = 0°$ and $\beta = 0°$ are shown in Fig. 16, with a comparison of $\theta_{DW} = 40°$ and $\theta_{DW} = -40°$ Similar to HCW, as the dihedral angle changes the variation of pressure distribution on the lower surface is more obvious than that on the upper surface. As the positive dihedral angle increases, the pressure difference between the upper and lower surfaces, as well as the normal or axial projected area, gradually decreases, causing a monotonically decreasing trend in the lift or drag coefficient. In contrast, as the negative dihedral angle of the delta wing increases, the pressure difference gradually increases, but the projected area decreases; thus, when the negative dihedral angle is small, the change in projected area is limited, and the pressure difference dominates the change of the lift or drag coefficient, i.e., the lift or drag coefficient will increase first until the negative dihedral angle exceeds a certain critical value. These explain the different trends induced by the changes of positive and negative dihedral angles observed in Fig. 9.

Further, considering the sideslip angle, we investigate the effect of the dihedral angle variation on flow field characteristics to reveal the change laws in lateral-directional stability as mentioned in Section 4.3.

For the HCW, Fig. 17 shows the pressure distribution on both the upper and lower surfaces at $\alpha = 0°$ and $\beta = 2°$, with a comparison between the results at $\theta_{HCW} = 20°, 0°, -20°$ Note that the positive sideslip angle β indicates that the incoming flow has a lateral component blowing from the left side of configurations to the right. As the dihedral angle changes the variation of pressure distribution on the lower surface is more obvious than that on the upper surface. When the incoming flow has a positive sideslip angle, the intensity on the left side of the body shock is stronger than that on the right.

Since the pressure distribution on the lower surface of HCW is mainly affected by the body shock, the overall level of pressure on the left side is higher than that on the right, regardless of the dihedral angle of HCW. However, the spanwise distribution of pressure from the middle to the left/right tips of HCW is changed as the dihedral angle varies. Fig. 17 also shows the pressure distributions acting along the left/right spanwise position at $X = 876mm$ (where the pressure change is significant) of the HCW lower surface. The results on the left and right sides are marked by the red and blue lines, respectively. ΔY represents the lateral distance from the symmetrical plane of HCW. If the HCW has a positive dihedral angle, as shown in Fig. 17(a), the pressure at different spanwise positions on the left side is almost always higher than that on the right, thus resulting in a rolling moment to enhance lateral stability. On the other hand, as depicted in Fig. 17(c), if the HCW has a negative dihedral angle, the spanwise pressure is higher on the left side near the HCW middle (i.e., $\Delta Y < 0.15$) than that on the right, while near the wing tip the spanwise pressure is higher on the right side. Since the moment arm is longer near the wing tip, part of the rolling recovery moment can be offset by the pressure on the right side, causing a deterioration of lateral stability.

For the delta wing, the pressure distribution on its lower surface, similar to HCW, exhibits a more pronounced variation as the dihedral angle changes, in contrast to that observed on the upper surface, as shown in Fig. 18. Differently, the pressure distributions on the left and right sides of the lower surface are strongly correlated with the dihedral angle. Specifically, a negative dihedral angle results in a higher pressure on the right side than that on the left, resulting in a deterioration of lateral stability. Conversely, a positive dihedral angle corresponds to a higher pressure on the left side, causing an enhancement of lateral stability.

Furthermore, if the delta wing has a negative dihedral angle, the pressure difference between its upper and lower surfaces is obviously greater on the right side than on the left. This generates a yaw moment that enhances directional stability. While a positive dihedral angle can also improve directional stability, its impact is weaker than that of a negative dihedral angle. This explains why increasing the negative dihedral angle of the delta wing is more effective in enhancing directional stability compared to increasing the positive dihedral angle, as observed in Fig. 12(b).

5. Conclusions

A parametric conceptual high-pressure capturing wing (HCW) configuration with dual lifting wings is designed in this study based on the basic principle of HCW aerodynamic configuration. Taking the dihedral angles of the delta wing and HCW as the design variables, combined with the uniform experimental design method, CFD techniques, and ordinary kriging surrogate algorithm, the effects of the wing dihedral angles on the hypersonic aerodynamic characteristics of the HCW configuration under different incoming flow states are investigated. The main conclusions are as follows:

(1) The lift-drag characteristics are mainly affected by the dihedral angle of the delta wing. When the positive dihedral angle of the delta wing increases, the lift coefficient, drag coefficient, and L/D will decrease monotonically; in contrast, when the negative angle increases, these lift-drag characteristic parameters will first
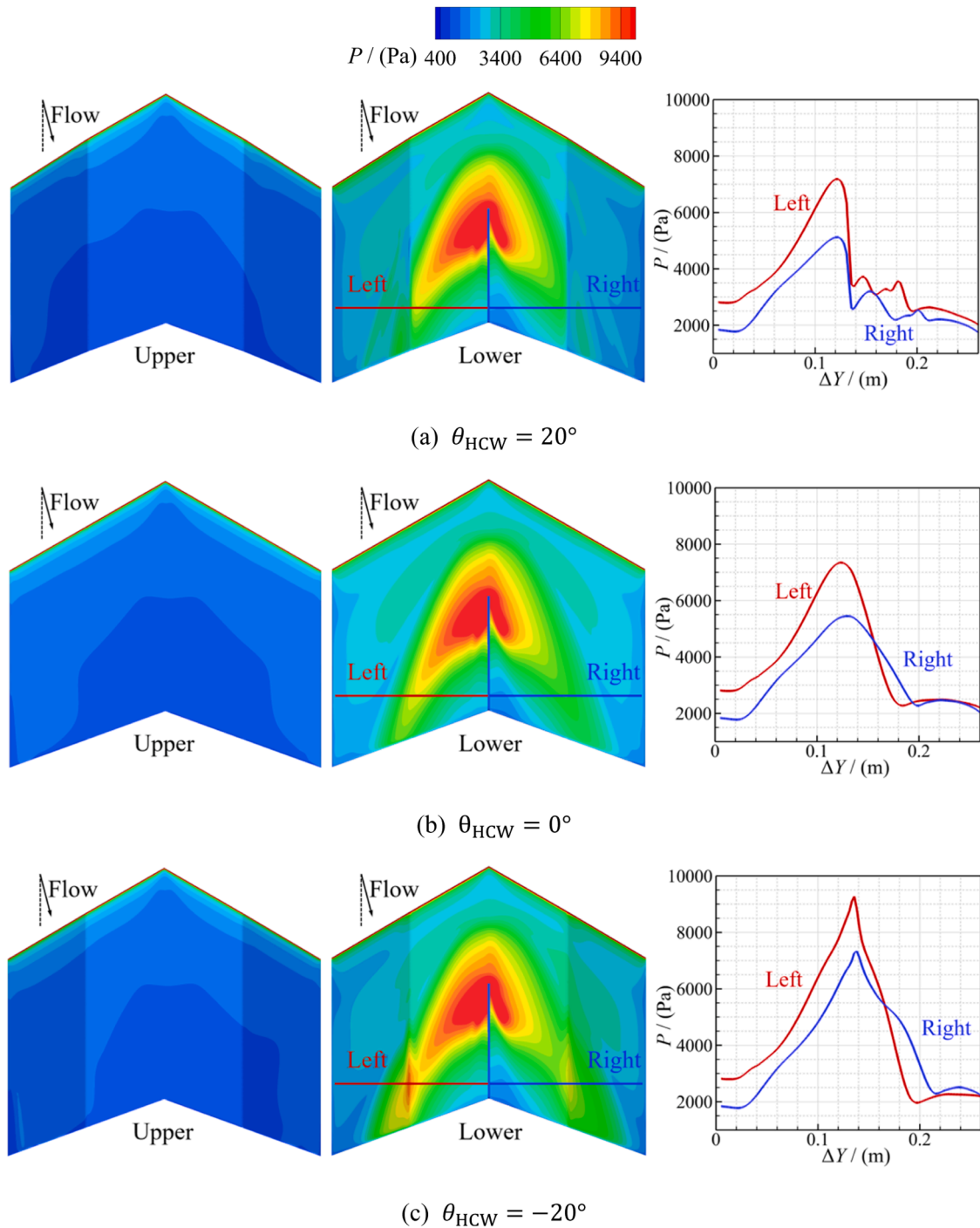
Fig. 17. Pressure contours on the upper and lower surfaces of HCW, and pressure distributions acting along the spanwise position at $X = 876$mm of the HCW lower surface, for the HCW configurations with different dihedral angles at $\alpha = 0°$ and $\beta = 2°$.

increase slightly and then decrease when a certain critical angle is exceeded. In particular, as the angle of attack increases, the sensitivity of L/D to the dihedral angles may decrease.

(2) The dihedral angle of HCW has a small effect on the longitudinal stability. When the delta wing has a positive dihedral angle, the longitudinal stability is slightly weakened; however, when the delta wing has a negative dihedral angle, the longitudinal stability is basically unchanged.

(3) The directional stability is enhanced, regardless of whether the dihedral angles of two wings are positive or negative, and the effect of negative angle (especially of the delta wing) is more obvious. As for the lateral stability, at small angles of attack, the positive dihedral angle of two wings enhances it, while the negative one weakens it. However, at large angles of attack, the lateral stability may be reduced if the positive dihedral angle of the delta wing is too large.

Declaration of Competing Interest

The authors declare that they have no known competing financial interests or personal relationships that could have appeared to influence the work reported in this paper.
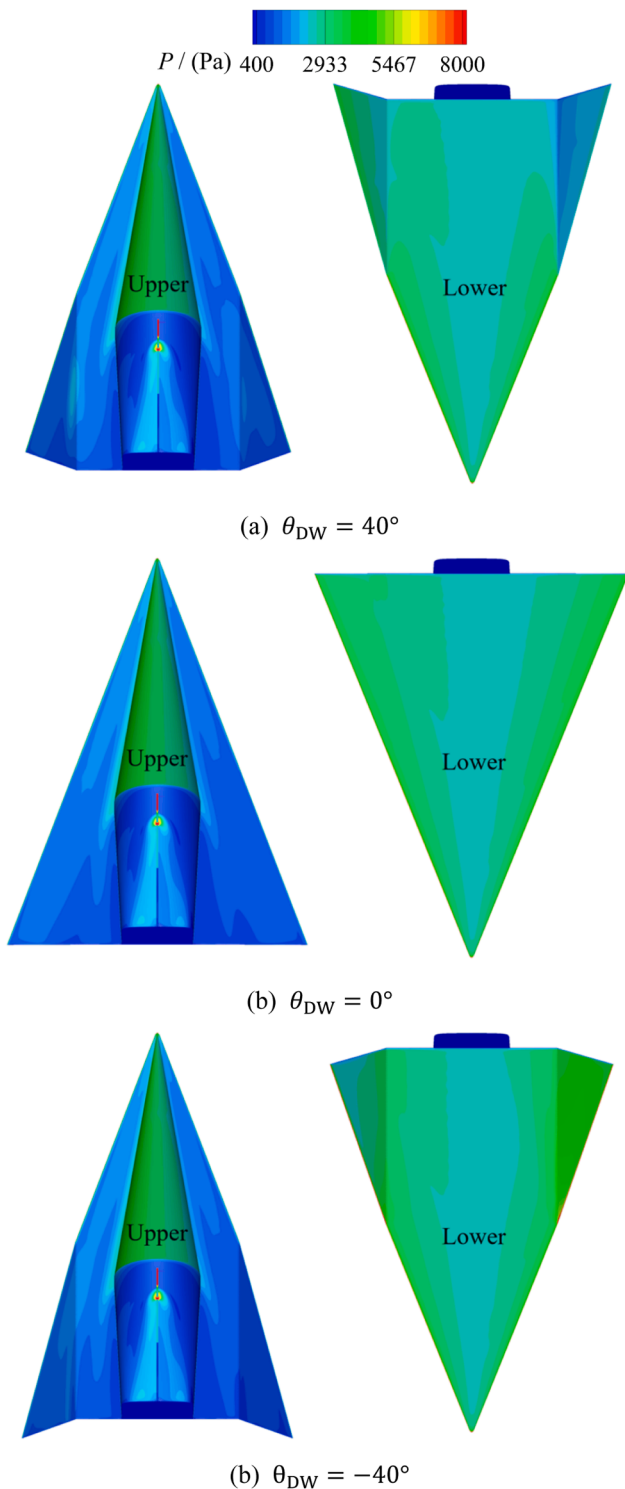
Fig. 18. Pressure contours on the upper and lower surfaces of the delta wing for the HCW configuration with different dihedral angles at $\alpha = 0°$ and $\beta = 2°$.

Data Availability

Data will be made available on request.

Acknowledgments

References

[1] F. Deng, F. Xie, N. Qin, et al., Drag reduction investigation for hypersonic lifting-body vehicles with aerospike and long penetration mode counterflowing jet, Aerosp. Sci. Technol. 76 (2018) 361–373.

[2] A. Viviani, L. Iuspa, A. Aprovitola, An optimization-based procedure for self-generation of *Re*-entry Vehicles shape, Aerosp. Sci. Technol. 68 (2017) 123–134.

[3] T. Sumimoto, K. Chiba, M. Kanazaki, et al., Evolutionary multidisciplinary design optimization of blended-wing-body-type flyback booster, in: AIAA Scitech 2019 Forum, 2019, p. 0703.

[4] F. Ding, J. Liu, C.B. Shen, et al., Novel approach for design of a waverider vehicle generated from axisymmetric supersonic flows past a pointed von Karman ogive, Aerosp. Sci. Technol. 42 (2015) 297–308.

[5] Y. Xiao, K. Cui, G.L. Li, et al., Preliminary study of aerodynamic performance for waverider-based hypersonic vehicles with dorsal mounted engines, in: 21st AIAA International Space Planes and Hypersonics Technologies Conference, 2017, p. 2315.

[6] F. Ding, J. Liu, C.B. Shen, et al., An overview of research on waverider design methodology, Acta Astronaut. 140 (2017) 190–205.

[7] F. Ding, J. Liu, C.B. Shen, et al., Experimental investigation of a novel airframe–inlet integrated full-waverider vehicle, AIAA J. 57 (7) (2019) 2964–2976.

[8] D. Küchemann, The Aerodynamic Design of aircraft, FRS, Pergamon Press, 1978.

[9] A. Viviani, L. Iuspa, A. Aprovitola, Multi-objective optimization for re-entry spacecraft conceptual design using a free-form shape generator, Aerosp. Sci. Technol. 71 (2017) 312–324.

[10] Y. Shen, W. Huang, L. Yan, et al., Constraint-based parameterization using FFD and multi-objective design optimization of a hypersonic vehicle, Aerosp. Sci. Technol. 100 (2020), 105788.

[11] K. Cui, G.L. Li, Y. Xiao, et al., Conceptual studies of the high pressure zone capture wing configuration for high speed air vehicles, Scientia Sinica (Physica, Mechanica Astronomica) 43 (5) (2013) 652–661.

[12] K. Cui, G.L. Li, Y. Xiao, et al., High-pressure capturing wing configurations, AIAA J. 55 (6) (2017) 1909–1919.

[13] K. Cui, Y. Xiao, Y.Z. Xu, et al., Hypersonic I-shaped aerodynamic configurations, Sci. China 61 (2) (2018).

[14] H.X. Wang, G.L. Li, Y.Z. XU, et al., Preliminary study on transonic flow characteristics of a high-pressure capturing wing configuration, Acta Aerodynam. Sinica 38 (3) (2020) 441–447.

[15] H.X. Wang, G.L. Li, J. Yang, et al., Numerical study on flow characteristics of high-pressure capturing wing configuration at subsonic, transonic and supersonic regime, Chinese J. Theoretical Appl. Mech. 53 (11) (2021) 3056–3070.

[16] H.X. Wang, Y. Xiao, K.K. Zhang, et al., Effect of body trailing edge shape on subsonic flow characteristics of high-pressure capturing wing configuration, Hangkong Xuebao 44 (6) (2023) 174–190.

[17] Y.L. Wang, Y.J. Wei, C. Wang, et al., Theoretical and numerical simulation study on aerodynamics of V configuration high-pressure capture wing (HCW-V), Phys. Fluids 34 (8) (2022), 086106.

[18] Y. Ma, W. Zhou, Q.L. Han, et al., Aerodynamic configuration of the HCW based on the lifting body, J. Aerosp. Eng. 32 (2) (2019), 04019004.

[19] G.L. Li, K. Cui, Y.Z. Xu, et al., Experimental investigation of a hypersonic I-shaped configuration with a waverider compression surface, Sci. China: Phys., Mech. Astron. 63 (5) (2020).

[20] R. Miller, B. Argrow, K. Center, et al., Experimental verification of the osculating cones method for two waverider forebodies at Mach 4 and 6, in: 36th AIAA Aerospace Sciences Meeting and Exhibit 682, 1998.

[21] T. Du, Y. Chen, Q.Y. Cai, et al., Research on aerodynamic configuration design principle for advanced hypersonic vehicle, Acta Aerodynamica. Sinica 33 (4) (2015) 501–509.

[22] S.Y. Chang, Z.W. Tian, G.L. Li, et al., Numerical study on longitudinal stability for HCW aircraft based on aerodynamic derivatives, Scientia Sinica Technolog. 53 (2023) 1–14.

[23] Q. Gao, Q. Li, Lateral-directional stability analysis of hypersonic vehicles of US, Cruising Missiles 12 (2012) 14–18.

[24] D. Dalle, S. Torrez, J. Driscoll, Sensitivity of flight dynamics of hypersonic vehicles to design parameters, in: 18th AIAA/3AF International Space Planes and Hypersonic Systems and Technologies Conference, 2012, p. 5909.

[25] G. Pezzella, M. Marini, M. Cicala, et al., Aerodynamic characterization of HEXAFLY scramjet propelled hypersonic vehicle, in: 32nd AIAA Applied Aerodynamics Conference, 2014, p. 2844.

[26] W. Liu, C.A. Zhang, X.P. Wang, et al., Parametric study on lateral–directional stability of hypersonic waverider, AIAA J. 59 (8) (2021) 3025–3042.

[27] C.Z. Liu, X.F. Meng, P. Bai, Design and analysis of double-swept waverider with wing dihedral, AIAA J. 60 (4) (2022) 2075–2084.

[28] A. Crasta, M.A. Baig, S.A. Khan, Estimation of stability derivatives of a delta wing in hypersonic flow, IJETED 6 (2) (2012) 505–516.

[29] T.X. Hu, Review of self-induced roll oscillations and its attenuation for low-aspect-ratio wings, Proc. Inst. Mech. Eng. Part G J. Aerosp. Eng. 233 (16) (2019) 5873–5895.

[30] Y. Yi, T.X. Hu, P.Q. Liu, et al., Dynamic lift characteristics of nonslender delta wing in large-amplitude-pitching, Aerosp. Sci. Technol. 105 (2020), 105937.

[31] Q.M. Chen, T.X. Hu, P.Q. Liu, et al., The dynamic vortical flow behaviour on a coplanar canard configuration during large-amplitude-pitching, Aerosp. Sci. Technol. 112 (2021), 106553.

[32] S. Tumse, I. Karasu, B. Sahin, Experimental investigation of ground effect on the vortical flow structure of a 40° swept delta wing, J. Aerosp. Eng. 35 (4) (2022), 04022055.

[33] S.Y. Chang, Y. Xiao, G.L. Li, et al., Effect of wing dihedral and anhedral angles on subsonic aerodynamic characteristics of HCW configuration, Chinese J. Theore. Appl. Mech. 54 (10) (2022) 2760–2772.

[34] K.T. Fang, D.K.J. Lin, P. Winker, et al., Uniform design: theory and application, Technometrics 42 (3) (2000) 237–248.

[35] K.T. Fang, D.K.J. Lin, Uniform experimental designs and their applications in industry, Handbook statistics 22 (2003) 131–170.

[36] P. Tian, G.L. Li, K. Cui, et al., Aerodynamic characteristics of high-pressure capturing wing configuration in multi-regime, Acta Aerodynam. Sinica 39 (3) (2021) 11–20.

[37] S. Chakravarthy, O. Peroomian, U. Goldberg, et al., The CFD++ computational fluid dynamics software suite, AIAA and SAE, in: 1998 World Aviation Conference, 1998, p. 5564.

[38] U. Goldberg, Hypersonic turbulent flow predictions using CFD++, in: AIAA/CIRA 13th International Space Planes and Hypersonics Systems and Technologies Conference, 2005, pp. 103–110.

[39] P. Dai, B. Yan, W. Huang, et al., Design and aerodynamic performance analysis of a variable-sweep-wing morphing waverider, Aerosp. Sci. Technol. 98 (2020), 105703.

[40] P.J. Roache, Perspective: a method for uniform reporting of grid refinement studies, J. Fluids Eng. 116 (3) (1994) 405–413.

[41] C. Bliamis, C. Menelaou, K. Yakinthos, Implementation of various-fidelity methods for viscous effects modeling on the design of a waverider, Aerosp. Sci. Technol. 133 (2023), 108141.

[42] P.J. Roache, Quantification of uncertainty in computational fluid dynamics, Annu. Rev. Fluid Mech 29 (1) (1997) 123–160.

[43] N. Cressie, Spatial prediction and ordinary kriging, Math. Geol. 20 (1988) 405–421.